
This copy is for your personal, non-commercial use only.

If you wish to distribute this article to others, you can order high-quality copies for your colleagues, clients, or customers by [clicking here](#).

Permission to republish or repurpose articles or portions of articles can be obtained by following the guidelines [here](#).

The following resources related to this article are available online at www.sciencemag.org (this information is current as of February 27, 2013):

Updated information and services, including high-resolution figures, can be found in the online version of this article at:

<http://www.sciencemag.org/content/315/5820/1843.full.html>

Supporting Online Material can be found at:

<http://www.sciencemag.org/content/suppl/2007/03/27/315.5820.1843.DC1.html>

This article **cites 25 articles**, 5 of which can be accessed free:

<http://www.sciencemag.org/content/315/5820/1843.full.html#ref-list-1>

This article has been **cited by** 67 article(s) on the ISI Web of Science

This article has been **cited by** 25 articles hosted by HighWire Press; see:

<http://www.sciencemag.org/content/315/5820/1843.full.html#related-urls>

This article appears in the following **subject collections**:

Ecology

<http://www.sciencemag.org/cgi/collection/ecology>

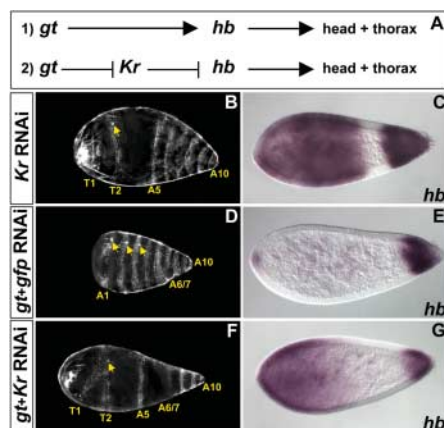


Fig. 4. Repression of *Nv-Kr* by maternal *Nv-gt* is required for head and thorax formation in *Nasonia*. (A) Two models for maternal *Nv-gt* function. Cuticular analysis (B, D, and F) and *Nv-hb_{zyg}* expression (C, E, and G) after knockdown for *Nv-Kr* [(B) and (C)], *Nv-gt+gfp* [(D) and (E)], and *Nv-gt+Kr* [(F) and (G)].

Nv-gt and green fluorescent protein (*gfp*) and observed the expected *Nv-gt* phenotype: deletion of head and thorax, as well as loss of anterior *Nv-hb* expression (Fig. 4, D and E). Knockdown of *Nv-gt* and *Nv-Kr* yielded striking results. In 92% of examined embryos, the head and thorax (T1/T2) were restored (Fig. 4F), and the resulting cuticular phenotypes were essentially identical to those after *Nv-Kr* RNAi alone (Fig. 4B). Consistent with rescued head and thorax development, anterior zygotic *Nv-hb* was also restored, although not to wild-type levels (Fig. 4G). Nonetheless, the amount of *Nv-hb* present in *Nv-gt+Kr* RNAi embryos was sufficient to direct head and thorax development, demonstrating that *Nv-Kr* expansion impedes anterior patterning and that maternally localized *Nv-gt* confines *Nv-Kr* to the embryo's center. Thus, whereas in *Drosophila*, *bcd*-activated *Dm-gt* plays only a moderate role in positioning *Nv-Kr* (Fig. 1C), in *Nasonia*, maternal *Nv-gt* is sufficient to perform this function. This distinction led us to consider whether *Dm-gt*'s role in *Drosophila* would be enhanced if the *Drosophila* embryo were reengineered to develop like *Nasonia*—with *Dm-gt* maternally provided and anteriorly localized. We found that, whereas *Dm-gt* was sufficient to repress *Dm-Kr* anteriorly in the absence of *bcd* (fig. S1B), head and thoracic structures were not rescued (fig. S1C)—an unsurprising result given that, in addition to permitting anterior development by regulating *Kr*-repressing gap genes, *bcd* also functions instructively to activate genes required for head and thorax formation. In *Nasonia*, by contrast, the instructive and permissive anterior patterning functions are discrete. Head- and thorax-specific genes are triggered by an instructive anterior determinant, maternal *Nv-otd1*, which is localized independently of the permissively acting maternal repression system, *Nv-gt*.

A comparison of the molecular mechanisms employed by two independently evolved (6) long-

germ insects not only uncovers those features essential to this developmental mode but also sheds light on how the *bcd*-dependent anterior patterning program might have evolved. Through analysis of the regulation of the trunk gap gene *Kr* in *Drosophila* and *Nasonia*, we have been able to demonstrate that anterior repression of *Kr* is essential for head and thorax formation and is a common feature of long-germ patterning. Both insects accomplish this task through maternal, anteriorly localized factors that either indirectly (*Drosophila*) or directly (*Nasonia*) repress *Kr* and, hence, trunk fates. In *Drosophila*, the terminal system and *bcd* regulate expression of gap genes, including *Dm-gt*, that repress *Dm-Kr*. *Nasonia*'s *bcd*-independent long-germ embryos must solve the same problem, but they employ a maternally localized repression system in which maternal *Nv-gt* is localized to the oocyte's anterior, where it represses *Nv-Kr*. In the dipteran lineage, whereas *gt* retained the ability to repress *Kr*, maternal regulation of *Kr*'s position was taken over by two novel features—*bcd*, a specific dipteran innovation, and the terminal pathway, which, although present ancestrally, appears to function less extensively in the anterior of non-dipteran insects (16, 17). In addition to activating anterior patterning genes such as *otd* and *hb*, *bcd* also acquired regulation of *gt*, which became a strictly zygotic gene with a reduced role in repressing *Kr*. Our findings thus identify two independent mechanisms for long-germ anterior patterning—one using two maternally localized genes, *otd1* and *gt*, that respectively activate anterior zygotic patterning genes and repress trunk fates, and a second using *bcd* for these same functions, thereby demoting *otd* and *gt* to zygotic gap genes. Interestingly, it appears that long-germ embryos use RNA localization for a number of different developmental processes (5, 18, 19). By contrast, in short-germ insects, although some localized RNAs have been identified, there is as yet no evidence of their contribution to anterior-posterior patterning (20).

mRNA localization indeed appears to be an important component of long-germ embryogenesis, perhaps even playing a role in the transition from the ancestral short-germ to the derived long-germ fate.

References and Notes

1. G. K. Davis, N. H. Patel, *Annu. Rev. Entomol.* **47**, 669 (2002).
2. T. Berleth *et al.*, *EMBO J.* **7**, 1749 (1988).
3. W. Driever, C. Nusslein-Volhard, *Cell* **54**, 83 (1988).
4. J. Lynch, C. Desplan, *Curr. Biol.* **13**, R557 (2003).
5. J. A. Lynch, A. E. Brent, D. S. Leaf, M. A. Pultz, C. Desplan, *Nature* **439**, 728 (2006).
6. J. Savard *et al.*, *Genome Res.* **16**, 1334 (2006).
7. G. Struhl, P. Johnston, P. A. Lawrence, *Cell* **69**, 237 (1992).
8. A. Preiss, U. B. Rosenberg, A. Kienlin, E. Seifert, H. Jackle, *Nature* **313**, 27 (1985).
9. M. Hulskamp, C. Pfeifle, D. Tautz, *Nature* **346**, 577 (1990).
10. X. Wu, R. Vakani, S. Small, *Development* **125**, 3765 (1998).
11. R. Kraut, M. Levine, *Development* **111**, 611 (1991).
12. J. A. Lynch, C. Desplan, *Nat. Protocols* **1**, 486 (2006).
13. R. Kraut, M. Levine, *Development* **111**, 601 (1991).
14. M. A. Pultz *et al.*, *Development* **132**, 3705 (2005).
15. G. F. Hewitt *et al.*, *Development* **126**, 1201 (1999).
16. J. A. Lynch, E. C. Olesnick, C. Desplan, *Dev. Genes Evol.* **216**, 493 (2006).
17. R. Schroder, C. Eckert, C. Wolff, D. Tautz, *Proc. Natl. Acad. Sci. U.S.A.* **97**, 6591 (2000).
18. E. C. Olesnick *et al.*, *Development* **133**, 3973 (2006).
19. A. Bashirullah, R. L. Cooperstock, H. D. Lipshitz, *Annu. Rev. Biochem.* **67**, 335 (1998).
20. G. Bucher, L. Farzana, S. J. Brown, M. Klingler, *Evol. Dev.* **7**, 142 (2005).
21. The authors wish to thank members of the Desplan and Small laboratories for support and advice. This project was supported by NIH grants GM64864, awarded to C.D., and GM51946, awarded to S.S. A.E.B. is a Damon Runyon Fellow, supported by the Damon Runyon Cancer Research Foundation (DRG-1870-05).

Supporting Online Material

www.sciencemag.org/cgi/content/full/315/5820/1841/DC1
 Materials and Methods

SOM Text

Fig. S1

References

13 November 2006; accepted 7 March 2007

10.1126/science.1137528

Emergent Biogeography of Microbial Communities in a Model Ocean

Michael J. Follows,^{1*} Stephanie Dutkiewicz,¹ Scott Grant,^{1,2} Sallie W. Chisholm³

A marine ecosystem model seeded with many phytoplankton types, whose physiological traits were randomly assigned from ranges defined by field and laboratory data, generated an emergent community structure and biogeography consistent with observed global phytoplankton distributions. The modeled organisms included types analogous to the marine cyanobacterium *Prochlorococcus*. Their emergent global distributions and physiological properties simultaneously correspond to observations. This flexible representation of community structure can be used to explore relations between ecosystems, biogeochemical cycles, and climate change.

A significant challenge in understanding the changing earth system is to quantify and model the role of ocean ecosystems in the global carbon cycle. The structure of microbial communities in the surface ocean is

known to regulate important biogeochemical pathways, including the efficiency of export of organic carbon to the deep ocean. Although there is extraordinary diversity in the oceans, the biomass of local microbial communities at

any location is typically dominated by a smaller subset of strains. Their relative fitness and ecosystem community structure are regulated by a variety of factors, including physical conditions, dispersal, predation, competition for resources, and the variability of the environment (1–3). Models reflecting this conceptual view have been examined in idealized ecological settings (4) and have been applied to studies of terrestrial ecosystems (5). We have used this approach in a marine ecosystem model that embraces the diversity of microbes and their genomic underpinnings, a model in which microbial community structure “emerges” from a wider set of possibilities and, thus, mimics aspects of the process of natural selection. The system is flexible enough to respond to changing ocean environments and can be used to interpret the structure and development of marine microbial communities and to reveal critical links between marine ecosystem structure, global biogeochemical cycles, and climate change.

Recent ocean models have begun to resolve community structure by the explicit representation of three or four classes, or functional groups, of phytoplankton (6–9), but significant challenges remain (10, 11). First, the specification of functional groups and diversity of the model ecosystem is subjective and somewhat arbitrary. Second, it is difficult to evaluate the parameters controlling such models because quantitative, physiological information from laboratory cultures is extremely limited. Third, observations of microbial community structure with which to evaluate global-scale models are still relatively sparse. Finally, model ecosystem structures optimized to reflect today’s ocean may not be sufficiently dynamic to adapt appropriately to a changing climate where radical shifts in community structure might be possible.

To circumvent some of these difficulties, we formulated a marine ecosystem model that represents a large number of potentially viable phytoplankton types whose physiological characteristics were determined stochastically. The initialized organism types interacted with one another and their environment, evolving into a sustainable ecosystem where community structure and diversity were not imposed, but were emergent properties.

The ecosystem model consisted of a set of coupled prognostic equations (eqs. S1 to S5), with idealized representations of the transformations of inorganic and organic forms of phosphorus, nitrogen, iron, and silica. Many tens of phytoplankton types (here, 78) were initialized in each simulation, each type distinguished by

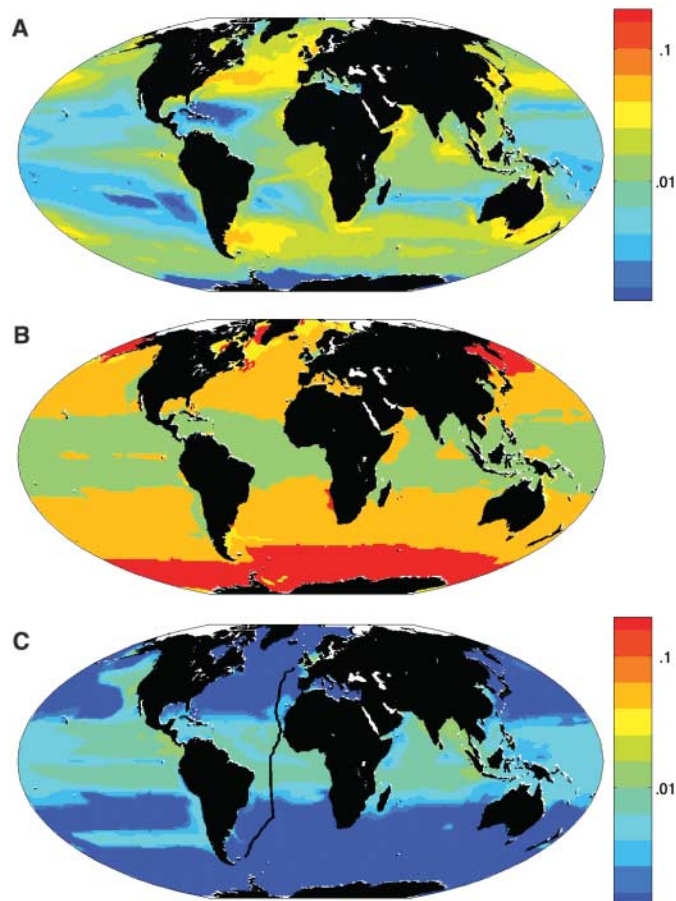
its physiological capabilities and the values of coefficients that control the rates and sensitivities of metabolic processes. These were provided by random drawing from broad ranges guided by laboratory and field studies (table S1). We focused these choices on light, temperature, and nutrient requirements (fig. S1), the niche dimensions for phytoplankton thought to be most important in regulating growth. To facilitate a test of the approach, we also specifically addressed functions that differentiate *Prochlorococcus* spp. from other phytoplankton, including their small size and inability to assimilate nitrate. Other functions could be emphasized depending on the aim of the study. Ecological trade-offs were imposed through highly simplified allometric constraints [see supporting online material (SOM)]. To reflect the extra energetic expense of using nitrate, relative to other inorganic nitrogen sources, we allowed the maximum growth rate to increase slightly when nitrate was not the major nitrogen source (12). Organisms incapable of utilizing nitrate were given a slightly lower nutrient half-saturation. We explicitly represented predation by two classes of grazer and, for the action of heterotrophic microbes, we used a simple remineralization rate (SOM).

A global ocean circulation model constrained by observations (13) provided flow fields and mixing coefficients that transport all biological

and chemical tracers. All phytoplankton types were initialized with identical distributions of biomass, and the model was integrated forward for 10 years, over which time a repeating annual cycle in ecosystem structure emerged. We repeated the integration 10 times, each time with a different random selection of phytoplankton physiologies, forming an ensemble of 10 members. Although each ensemble member produced a unique emergent ecosystem, the broad-scale patterns of productivity, community structure, and biogeography were robust across all 10. Global patterns of open-ocean biomass (Fig. 1A), primary production, and nutrients (fig. S3) were qualitatively consistent with in situ and remote observations. The ensemble mean globally integrated, annual primary production was 44 gigatons C per year, with a standard deviation of less than 5%. This small standard deviation suggested that sufficient phytoplankton “types” were initialized for consistent emergent solutions and also reflects the large-scale regulation by the physical transport of nutrients.

After an initial adjustment, the biomass of some phytoplankton types fell below the threshold of numerical noise, and these types were assumed to have become “extinct.” In all ensemble members, about 20 phytoplankton types accounted for almost all of the total global biomass (fig. S2). We classified the phytoplankton types into four broad functional groups, each a

Fig. 1. Annual mean biomass and biogeography from single integration. (A) Total phytoplankton biomass ($\mu\text{M P}$, 0 to 50 m average). (B) Emergent biogeography: Modeled photo-autotrophs were categorized into four functional groups; color coding is according to group locally dominating annual mean biomass. Green, analogs of *Prochlorococcus*; orange, other small photo-autotrophs; red, diatoms; and yellow, other large phytoplankton. (C) Total biomass of *Prochlorococcus* analogs ($\mu\text{M P}$, 0 to 50 m average). Black line indicates the track of AMT13.



¹Department of Earth, Atmospheric and Planetary Sciences, Massachusetts Institute of Technology, 54-1514 MIT, Cambridge, MA 02139, USA. ²Department of Oceanography, University of Hawaii, 1000 Pope Road, Honolulu, HI 96822, USA. ³Departments of Civil and Environmental Engineering and Biology, Massachusetts Institute of Technology, 48-419 MIT, Cambridge, MA 02139, USA

*To whom correspondence should be addressed. E-mail: mick@mit.edu

composite of several types, according to aspects of their physiology: (i) diatom analogs—large phytoplankton that require silica, (ii) other large eukaryotes, (iii) *Prochlorococcus* analogs—small phytoplankton that cannot assimilate nitrate, and (iv) other small photo-autotrophs. The large-scale biogeography of the emergent phytoplankton community was plausible with respect to observations (Fig. 1B) and consistent among the 10 ensemble members. The model successfully captured the domination of annual biomass by large phytoplankton in subpolar upwelling regions, where both light and macronutrients are seasonally plentiful. The subtropical oceans were dominated by small phytoplankton functional types (14). Large areas of the tropics and subtropics were dominated by several *Prochlorococcus* analogs (Fig. 1C), also in accord with observations (15, 16). Along the cruise track of Atlantic Meridional Transect 13 (AMT13), total *Prochlorococcus* abundance (the sum of all

Prochlorococcus analogs) qualitatively and quantitatively reflected the major features of the observed distribution with highest abundances in the most oligotrophic (nutrient-depleted) waters (15, 17) (Fig. 2, A to D).

Real-world *Prochlorococcus* exhibit genetic diversity, which leads to differences in light and temperature sensitivities (17–20), as well as nitrogen assimilation abilities (21). The strains, or ecotypes, of *Prochlorococcus* exhibit distinct patterns of abundance along ocean gradients (15, 17), and observations on AMT13 (17) (Fig. 2, E, G, I, and K) provide an ideal test for the stochastic modeling strategy: Do the emergent model analogs of *Prochlorococcus* reflect the geographic distributions, relative abundances, and physiological properties of their real-world counterparts?

Of the *Prochlorococcus* analogs initialized in each model solution, between three and six variants persisted with significant abundances (fig. S4). We grouped the analogs by defining three

“model ecotypes” based only on distinct geographic habitats, without regard to physiology, which had a qualitative resemblance to the observed distributions of ecotypes along AMT13. In any ensemble member, more than one emergent *Prochlorococcus* analog may fall into a particular model-ecotype classification, and some were ambiguous. Model ecotype *m-e1* (Fig. 2F) was defined to include emergent analogs with significant biomass in the upper 25 m along the transect between 15°N and 15°S, qualitatively corresponding to the habitat of real-world ecotype eMIT9312 (Fig. 2E). Model ecotype *m-e2* (Fig. 2H) included analogs that had significant biomass in surface waters polewards of 15° but low biomass within 15° of the equator, broadly reflecting eMED4 (Fig. 2G). Finally, model ecotype *m-e3* (Fig. 2J) was defined to include analogs that had a subsurface maximum biomass, in common with eMIT9313 and eNATL2A (Fig. 2, I and K). The observed widespread distribution of deep maxima with low abundance associated with eMIT9313 and eNATL2A was not clearly reflected in the model analogs. This might be explained by the tendency toward unrealistically complete competitive exclusion typical in ecosystem models (22, 23), precluding persistent populations at low abundance. There is a deep, high biomass layer in the model made up of other, nitrate-consuming, small phytoplankton. This may partially reflect a contribution from nitrate-utilizing *Prochlorococcus*, which have recently been inferred from ocean observations (24), but which have not yet been seen in culture.

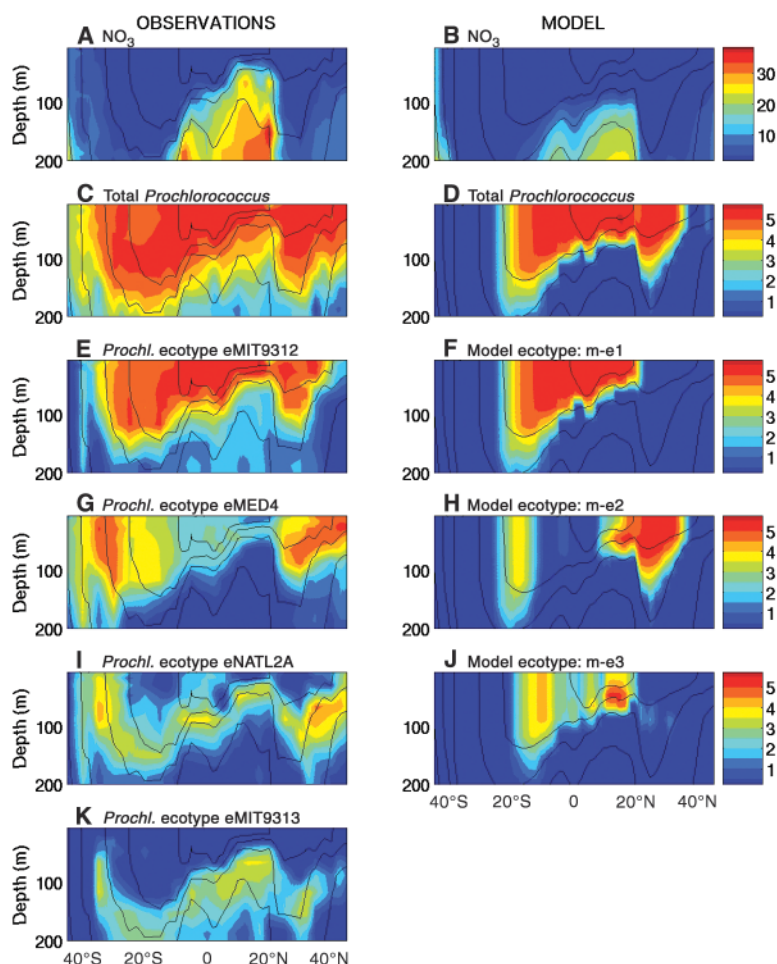


Fig. 2. Observed and modeled properties along the AMT13 cruise track. Left column shows observations (17), right column shows results from a single model integration. (A and B) Nitrate ($\mu\text{mol kg}^{-1}$); (C and D) total *Prochlorococcus* abundance [$\log (\text{cells ml}^{-1})$]. (E, G, I, and K) Distributions of the four most abundant *Prochlorococcus* ecotypes [$\log (\text{cells ml}^{-1})$] ranked vertically. (F, H, and J) The three emergent model ecotypes ranked vertically by abundance. Model *Prochlorococcus* biomass was converted to cell density assuming a quota of 1 fg P cell^{-1} (27). Black lines indicate isotherms.

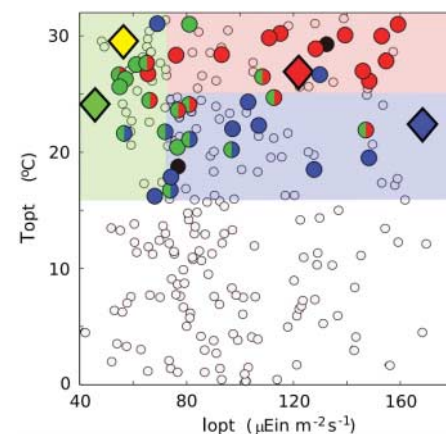


Fig. 3. Optimum temperature and light intensity for growth, T_{opt} and I_{opt} , of all initialized *Prochlorococcus* analogs (all circles) from the ensemble of 10 model integrations. Large circles indicate the analogs that exceeded a total biomass of 10^6 mol P along AMT13 in the 10th year. Colors indicate classification into model ecotypes (see main text): Red circles, *m-e1*; blue circles, *m-e2*; green circles, *m-e3*. Mixed-color and solid black circles denote ambiguity in model-ecotype classification. Bold diamonds indicate real-world *Prochlorococcus* ecotypes (red, eMIT9312; blue, eMED4; green, eNATL2A; and yellow, eMIT9313).

Within each ensemble member, emergent model ecotypes typically followed the abundance ranking of their geographically identified real-world counterparts (Fig. 2 and fig. S4): Model ecotypes *m-e1* and *m-e2* ranked first and second (compare these with eMIT9312 and eMED4, respectively), with *m-e3* consistently at lower abundances (compare this with ecotypes eNATL2A and eMIT9313).

There is a simultaneous correspondence between the physiological characteristics of emergent, modeled ecotypes and cultured representatives of the wild population. Each cultured strain of *Prochlorococcus* and the emergent model ecotypes from all 10 ensemble members were characterized by an optimal temperature (T_{opt}) and photon flux (I_{opt}) for growth, the temperature or light intensity at which growth rates are greatest if all other limitations are set aside (fig. S1). Potentially viable *Prochlorococcus* analogs were seeded in the model over wide ranges of optimal temperature and photon fluxes (all circles, Fig. 3), but those that maintained significant abundances along the AMT transect (solid large circles, Fig. 3) were all characterized by $T_{opt} > 15^{\circ}\text{C}$. This is consistent with the observations of *Prochlorococcus* in warmer waters and with the warm T_{opt} of cultured strains (17). Our model indicates that the oligotrophic conditions confined *Prochlorococcus* analogs to warmer waters and selected for warm T_{opt} , an emergent “adaptation” driven by other environmental factors. In the cooler waters of the model, nutrients are typically abundant, and so larger phytoplankton, with higher intrinsic maximum growth rates, have an advantage. In the highly oligotrophic (typically warmer) regions, the *Prochlorococcus* analogs’ lower half-saturation (consistent with their very small size) is advantageous.

Across the ensemble of 10 integrations, the geographically defined model ecotypes were clustered in optimal temperature and light parameter space (Fig. 3): Model ecotype *m-e1* (red circles) generally occupied the warmest area of parameter space over a broad, upper range of optimal photon fluxes; *m-e2* (blue circles) generally had a lower T_{opt} but a similar range of I_{opt} . This is consistent with their surface-oriented habitats and latitudinal (or temperature) separation. In contrast, *m-e3* (green circles) occupied a wider range of T_{opt} but only in the region of lowest I_{opt} , consistent with its expression of subsurface maxima. Although there were exceptions, the clustering of geographically defined model ecotypes in physiological parameter space indicated that robust ecological controls were operating across the 10 integrations. The physiological characteristics (T_{opt} , I_{opt}) of real-world ecotypes (colored diamonds, Fig. 3) are notably consistent with the grouping of their model counterparts. This correspondence was not imposed, but emerged as a feature of the model solution.

Significantly, there was simultaneous consistency between the geographical habitat, rank abundance, and physiological specialization of the

emergent *Prochlorococcus* model ecotypes and their real-world counterparts. These parallels indicate that the stochastic, self-organizing representation of marine ecosystems reflects real-world processes and is suitable for application in ecological and biogeochemical studies. This approach circumvents some of the obstacles facing most current ocean ecosystem models, such as the a priori imposition of low diversity, the prescription of dominant functional types, and the difficulty of specifying the physiological rate coefficients that define them. This function-based approach can naturally evolve to exploit the growing body of genomic and metagenomic data mapping the oceans in terms of genes and their encoded physiological functionality (25, 26). Finally, because the ecosystem structure and function are, by design, emergent and not tightly prescribed, this modeling approach is ideally suited for studies of the relations between marine ecosystems, evolution, biogeochemical cycles, and past and future climate change.

References and Notes

1. D. Tilman, *Ecology* **58**, 338 (1977).
2. R. Margalef, *Perspectives in Ecological Theory* (Univ. of Chicago Press, Chicago, 1968).
3. C. Pedrós-Alió, *Trends Microbiol.* **14**, 257 (2006).
4. S. L. Pimm, J. H. Lawton, *Nature* **268**, 329 (1977).
5. A. Kleidon, H. A. Mooney, *Glob. Change Biol.* **6**, 507 (2000).
6. J. K. Moore, S. Doney, J. Kleyplas, D. Glover, I. Fung, *Deep-Sea Res. II* **49**, 403 (2001).
7. W. W. Gregg, P. Ginoux, P. S. Schopf, N. W. Casey, *Deep-Sea Res. II* **50**, 3143 (2003).
8. E. Litchman, C. A. Klausmeier, J. R. Miller, O. M. Schofield, P. G. Falkowski, *Biogeosciences* **3**, 585 (2006).
9. C. LeQuere *et al.*, *Glob. Change Biol.* **11**, 2016 (2006).
10. T. R. Anderson, *J. Plankton Res.* **27**, 1073 (2005).
11. R. R. Hood *et al.*, *Deep-Sea Res. II* **53**, 459 (2006).
12. P. A. Thompson *et al.*, *Limnol. Oceanogr.* **34**, 1014 (1989).
13. C. Wunsch, P. Heimbach, *Physica D* **10.1016/j.physd.2006.09.040** (2006).
14. Y. Dandonneau, Y. Montel, J. Blanchot, J. Giraudeau, J. Neveux, *Deep-Sea Res. I* **53**, 689 (2006).
15. M. V. Zubkov, M. A. Sleight, P. H. Burkitt, R. J. G. Leakey, *Prog. Oceanogr.* **45**, 369 (2000).
16. H. A. Bouman *et al.*, *Science* **312**, 918 (2006).
17. Z. I. Johnson *et al.*, *Science* **311**, 1737 (2006).
18. L. R. Moore, G. Rocap, S. W. Chisholm, *Nature* **393**, 464 (1998).
19. G. Rocap *et al.*, *Nature* **424**, 1042 (2003).
20. L. R. Moore, S. W. Chisholm, *Limnol. Oceanogr.* **44**, 628 (1999).
21. L. R. Moore, A. F. Post, G. Rocap, S. W. Chisholm, *Limnol. Oceanogr.* **47**, 989 (2002).
22. G. E. Hutchinson, *Am. Nat.* **95**, 137 (1961).
23. R. A. Armstrong, R. McGehee, *Am. Nat.* **115**, 151 (1980).
24. M. W. Lomas, F. Lipschultz, *Limnol. Oceanogr.* **51**, 2453 (2006).
25. J. C. Venter *et al.*, *Science* **304**, 66 (2004).
26. E. F. DeLong *et al.*, *Science* **311**, 496 (2006).
27. S. Bertilsson, O. Berglund, D. M. Karl, S. W. Chisholm, *Limnol. Oceanogr.* **48**, 1721 (2003).
28. Thanks to J. Marshall, R. Williams, P. Falkowski, J. Cullen, and J. Bragg for inspiration and encouragement. Thanks also to M. Coleman, R. Hood, and three anonymous reviewers for stimulating comments on the manuscript; to C. Hill for computing guidance; and to P. Heimbach, C. Wunsch, and the ECCO group for ocean circulation state estimates. We are grateful for funding from the PARADIGM consortium of the National Ocean Partnership Program, NSF (M.J.F., S.D.), NSF, DOE (S.W.C.), and the Gordon and Betty Moore Foundation (S.W.C., M.J.F.). M.J.F. is also grateful for the MIT Global Habitat Longevity Award. We acknowledge the Atlantic Meridional Transect consortium (NER/O/S/2001/00680), which enabled the biogeographical observations first published in (17) (AMT contribution no. 107).

Supporting Online Material

www.sciencemag.org/cgi/content/full/315/5820/1843/DC1

Materials and Methods

SOM Text

Figs. S1 to S4

Table S1

References and Notes

7 December 2006; accepted 5 March 2007

10.1126/science.1138544

Cascading Effects of the Loss of Apex Predatory Sharks from a Coastal Ocean

Ransom A. Myers,¹ Julia K. Baum,^{1*} Travis D. Shepherd,¹ Sean P. Powers,² Charles H. Peterson^{3*}

Impacts of chronic overfishing are evident in population depletions worldwide, yet indirect ecosystem effects induced by predator removal from oceanic food webs remain unpredictable. As abundances of all 11 great sharks that consume other elasmobranchs (rays, skates, and small sharks) fell over the past 35 years, 12 of 14 of these prey species increased in coastal northwest Atlantic ecosystems. Effects of this community restructuring have cascaded downward from the cownose ray, whose enhanced predation on its bay scallop prey was sufficient to terminate a century-long scallop fishery. Analogous top-down effects may be a predictable consequence of eliminating entire functional groups of predators.

Ecological impacts of eliminating top predators can be far-reaching (1) and include release of mesopredator prey populations

from predatory control (2) and induction of subsequent cascades of indirect trophic interactions (3–5). In the oceans, fishing has disproportional



Supporting Online Material for
Emergent Biogeography of Microbial Communities in a Model Ocean

Michael J. Follows,^{*} Stephanie Dutkiewicz, Scott Grant, Sallie W. Chisholm

^{*}To whom correspondence should be addressed. E-mail: mick@mit.edu

Published 30 March 2007, *Science* **315**, 1843 (2007)
DOI: 10.1126/science.1138544

This PDF file includes

Materials and Methods
SOM Text
Figs. S1 to S4
Table S1
References

Supporting Online Material

METHODS:

S1. Ecosystem Model Algorithms.

We formulate the ecosystem model in a generalized framework which represents an arbitrary number of nutrients, N_i , phytoplankton types, P_j , and grazers, Z_{ki} . Each nutrient element also has an associated particulate organic and dissolved organic matter pool, POM_i and DOM_i respectively. The rates of change of these prognostic variables are described by the following set of equations:

$$\frac{\partial N_i}{\partial t} + \nabla \cdot (u N_i) = \nabla \cdot (\kappa \nabla N_i) - \sum_j [\mu_j \gamma_j^T \gamma_j^I \gamma_j^N P_j R_{ij}] + S_i \quad (S1)$$

$$\frac{\partial P_j}{\partial t} + \nabla \cdot (u P_j) = \nabla \cdot (\kappa \nabla P_j) + \mu_j \gamma_j^T \gamma_j^I \gamma_j^N P_j - \frac{\partial (w_j^P P_j)}{\partial z} - m_j^P P_j - \sum_k g_{jk} \frac{P_j}{P_j + k_j^P} Z_{k,i=1} \quad (S2)$$

$$\frac{\partial Z_{ki}}{\partial t} + \nabla \cdot (u Z_{ki}) = \nabla \cdot (\kappa \nabla Z_{ki}) + Z_{ki} \sum_j g_{jk} R_{ij} \frac{P_j}{P_j + k_j^P} - m_k^Z Z_{ki} \quad (S3)$$

$$\frac{\partial POM_i}{\partial t} + \nabla \cdot (u POM_i) = \nabla \cdot (\kappa \nabla POM_i) - r_{POi} POM_i - \frac{\partial (w_{POM} POM_i)}{\partial z} + S_{POMi} \quad (S4)$$

$$\frac{\partial DOM_i}{\partial t} + \nabla \cdot (u DOM_i) = \nabla \cdot (\kappa \nabla DOM_i) - r_{DOi} DOM_i + S_{DOMi} \quad (S5)$$

Symbols are defined in the text below and parameter values or ranges are provided in Table S1. Units are $\mu\text{M P}$ for Eq. S2, and $\mu\text{M P}$, $\mu\text{M N}$, $\mu\text{M Si}$, or $\mu\text{M Fe}$ (element represented by subscript i) for Eqs. S1, S3, S4 and S5. Here R_{ij} denotes the ratio of element, i , relative to phosphorus, for each phytoplankton type, j . Separate zooplankton pools are carried for each element, Z_{ki} , where k is the zooplankton type and i the nutrient element, accounting for the ingestion of prey with different elemental ratios. Subscript $i=1$ refers to phosphorus.

Tracers are transported by the currents, u , and mixing coefficients, κ , from the ECCO (“Estimating the Circulation and Climate of the Ocean”) state estimate of ocean circulation (S1) based on a moderate resolution ($1^\circ \times 1^\circ$, 23 vertical levels), global configuration of the MIT ocean

circulation model (S2) constrained to be consistent with observations of large-scale hydrography and altimetry. Nutrient distributions are initialized from observed climatologies (S3) or previous simulations (S4).

S1.1 Parameterizations of Phytoplankton Physiology

While the approach to the organization and complexity of the ecosystem model are novel, the idealized descriptions of phytoplankton physiological processes are similar to those applied in previous studies (S4-S7). Phytoplankton growth is determined by a maximum intrinsic growth rate, μ_j , modulated by non-dimensional factors which reflect sensitivities to ambient temperature, photon flux and essential nutrients (Fig. S1). Nutrient limitation of growth is determined by the most limiting resource,

$$\gamma_j^N = \phi \min(N_1^{\text{lim}}, N_2^{\text{lim}}, \dots) \quad (\text{S6})$$

where the nutrients considered are phosphate, iron, silicic acid and nitrate, nitrite and ammonia. The effect on growth rate of ambient phosphate, iron or silicic acid concentrations is represented by a Michaelis-Menton function

$$N_i^{\text{lim}} = \frac{N_i}{N_i + k_{ij}} \quad (\text{S7})$$

where the K_{ij} are half-saturation constants for phytoplankton type j with respect to the ambient concentration of nutrient i (Fig. S1C). We resolve three potential sources of inorganic nitrogen (ammonia, nitrite and nitrate) though modeled phytoplankton may be able to assimilate ammonia only, ammonia and nitrite, or all three (S8). Since it is energetically more expensive to utilize nitrate relative to the other sources we represent nitrogen limitation by the following function:

$$N_N^{\text{lim}} = \frac{NO_3}{NO_3 + k_{NO_3j}} e^{-\psi NH_4 - \psi NO_2} + \frac{NO_2}{NO_2 + k_{NO_2j}} e^{-\psi NH_4} + \frac{NH_4}{NH_4 + k_{NH_4j}} \quad (\text{S8})$$

where ψ reflects the inhibition of nitrate or nitrite uptake (S9). Growth rate is enhanced when utilizing only ammonia, or ammonia and nitrite:

$$\phi = \left(\nu + (1 - \nu) \left(NO_2^{\text{lim}} + NH_4^{\text{lim}} \right) / N_N^{\text{lim}} \right) \quad (\text{S9})$$

where NO_2^{lim} and NH_4^{lim} represent the second and third terms on the right of Eq. S8. A phytoplankton type utilizing only nitrate thus has growth rate reduced by a factor ν relative to one using no nitrate (S10).

Temperature modulation of growth is represented by a non-dimensional factor

$$\gamma_j^T = \frac{1}{\tau_1} \left(A^T e^{-B(T-T_0)^C} - \tau_2 \right) \quad (S10)$$

which sets a temperature range over which each phytoplankton type can grow efficiently (Fig. S1A), and there is a general decrease in growth efficiency with temperature (S11). Coefficients τ_1 and τ_2 normalize the maximum value, while A , B , T_0 , and C regulate the form of the sensitivity envelope.

We incorporate a very simple radiative transfer model (S4) which captures self-shading but does not resolve spectral bands. The light sensitivity of growth rate is parameterized using the function (S12):

$$\gamma_j^I = \frac{1}{F_{\max}} \left(1 - e^{-k_{PAR} I} \right) e^{-k_{inhib} I} \quad (S11)$$

where $I(z)$ is the local, vertical flux of photosynthetically active radiation, PAR, and

$$F_{\max} = \frac{k_{PAR} + k_{inhib}}{k_{PAR}} \exp \left(-\frac{k_{inhib}}{k_{PAR}} \ln \left(\frac{k_{inhib}}{k_{PAR} + k_{inhib}} \right) \right)$$

is chosen to normalize the maximum value of γ_j^I to 1 (Fig. S1B). The parameter k_{par} defines the increase of growth rate with light at low levels of irradiation while k_{inhib} regulates the rapidity of the decline of growth efficiency at high PAR, or photo-inhibition (S12). This highly idealized parameterization of light sensitivity captures variations in optimal light intensity, and their ecological implications, but does not explicitly account for photo-acclimation, differences in accessory pigments and other factors which might lead to variability in the maximum light dependent growth factor. We note that, while the function γ_j^I is normalized to a maximum value of 1 for all phytoplankton types, large size-class phytoplankton are given a higher maximum intrinsic growth rate, μ_j .

We impose fixed elemental ratios for each phytoplankton type, R_{ij} , though these may vary between types (e.g. some require silica while others do not). To restrict the niche dimension and computational expense of this initial study, we have imposed an average, Redfieldian N:P stoichiometry of 16:1 for all phytoplankton types. We note that in nature elemental ratios are flexible and *Prochlorococcus*, for example, can significantly exceed this value (S13). Formulating the model with dynamic nutrient quotas would capture flexible stoichiometry and is more physiologically appropriate (S14,S15) but also would significantly increase the number of three-

dimensional arrays required to describe each phytoplankton type, dramatically increasing the computational expense. Hence we have not used this approach in this initial illustration.

SI.2 Assignment of Physiological Functionality and Growth Rate Sensitivities.

At the heart of this modeling strategy is the self-organization of a stochastically generated phytoplankton community. The physiological functionality and sensitivity of growth to temperature, light and ambient nutrient abundance for each modeled phytoplankton type is governed by several true/false parameters, the values of which are based on a virtual “coin-toss” at the initialization of each phytoplankton type. These determine the size class of each phytoplankton type (“large” or “small”), whether the organism can assimilate nitrate, whether the organism can assimilate nitrite, and whether the organism requires silicic acid. Parameter values which regulate the effect of temperature, light and nutrient availability on growth, are then assigned stochastically. T_o , which controls the optimum temperature for growth, and K_{PO_4} , the phosphate half-saturation coefficient (to which other half-saturations are indexed by the fixed elemental ratios), are drawn from prescribed ranges using a random number generator. Values for k_{par} and k_{inhib} are also randomly chosen, drawn from prescribed normal distributions. Some simple allometric trade-offs are imposed (Fig. S1): Phytoplankton in the large size class are distinguished by higher intrinsic maximum growth rates and faster sinking speeds (S16). They also draw parameter values from distributions with higher nutrient half-saturations (assuming they are less efficient at acquiring nutrients, S17) and are assumed to be high-light adapted due to packaging effects (S18, S19). These trade-offs are implemented by randomly selecting parameter values from different (though overlapping) distributions for large and small phytoplankton.

We note that, since the values of the governing coefficients are initialized stochastically from given distributions rather than prescribed specifically for each phytoplankton functional type, the total number of externally prescribed parameters in this approach (Table S1) is the same whether 10 or 10,000 phytoplankton types are initialized. The diversity of the “successful” population, and the parameter values that govern those organisms, are self-selected during the initial adjustment of the ecosystem model.

SI.3 Grazing, Mortality, Remineralization and Biogeochemical Cycles.

Parameterizations of grazing and other forms of heterotrophy are simplified in this study, which focuses on complexity and selection in the photo-autotrophs. None of the parameters regulating grazing and remineralization processes are stochastic in the simulations presented here. We prescribe a simple grazer community with two size classes. Large zooplankton preferentially graze (g_{fast}) on large phytoplankton, but can graze on small phytoplankton (g_{slow}) and visa versa for small zooplankton. A half-saturation coefficient (K^P) regulates grazing efficiency at high prey concentrations. Excretion and non-grazing mortality are represented as linear loss terms for both phytoplankton and grazers, with coefficients m^p and m^z respectively. This simplified, low diversity grazer community is chosen to facilitate a computationally and intellectually tractable study in this initial illustration. Future studies should examine, for example, a greater diversity of grazers with a variety of stochastically appointed feeding strategies broadening the general strategy to include the next trophic level.

The term S_i (Eq. S1) represents the source of inorganic nutrient due to the remineralization of organic forms as well as external sources and non-biological transformations (S4, S17). Heterotrophic microbes are not explicitly represented and the remineralization of dissolved and particulate organic detritus pools is treated as a simple linear decay with respective prescribed timescales $1/r_{POMi}$ and $1/r_{DOMi}$ (S4). S_{POMi} (Eq. S4) and S_{DOMi} (Eq. S5) are the sources of particulate and dissolved organic detritus arising from mortality and excretion of all phytoplankton types and

grazers (in Eq. S2 and S3), closing the nutrient budgets. Here we simply define a fixed fraction (f_{DOM}) of mortality and excretion to pass into each organic detritus pool, assuming that large phytoplankton and zooplankton contribute a larger fraction of their detritus to the POM_i pool than do the small phytoplankton. All silica is assumed to go to a POM pool, there is no dissolved organic silica.

The remineralization of organic phosphorus and iron produce phosphate and dissolved iron respectively, while the remineralization of organic nitrogen is assumed to produce ammonia which may then be nitrified to nitrite and, subsequently, nitrate. The microbial process of nitrification is also treated simply as first order reactions with fixed rate coefficients (ζ_{NO_2} , ζ_{NO_3}) resulting in qualitatively reasonable distributions of the nitrogen species. Due to the relatively short timescale of the integrations and to restrict the complexity of this initial study we do not represent diazotrophy. Simplified one dimensional studies indicate that enabling diazotrophy as a possible functionality for the modeled phytoplankton types enhances the availability of more reduced forms of nitrogen in the subtropical regions resulting in an increase the abundance of *Prochlorococcus* analogs.

Iron chemistry in seawater is parameterized (S20) with a complexation to an organic ligand (binding strength, β_{Fe}) and scavenging to falling particles (rate, c_{fe}). Dust (S21) deposited in the surface (solubility, α_{fe}) is a source of iron.

SUPPORTING TEXT

S2. Supplementary Model Results.

An ensemble of model integrations was performed, each with a different randomization of physiological characteristics but identical initialization and physical environment. 78 phytoplankton types were initialized in each integration: Experimentation suggested that the modeled community structure would be less robust with fewer than 30, and practical computational considerations placed an upper limit at 78. Computational cost also limited the ensemble to only 10 members. Fig. S2 shows the annual mean concentration, at year 10, of phosphorus in biomass of the 78 phytoplankton from a single ensemble member. All ensemble members exhibit a similar set of occupied habitats which are collectively reminiscent of the previously proposed biogeographical provinces (S22). All ensemble members produce very similar total primary production and nutrient fields (shown for one member in Fig. S3), and these compare favorably to observations. The similarity in the total primary production reflects the significant regulation of physical nutrient supply and light on gyre and basin scales.

The general biogeography of the model (depicted for a single ensemble member in Fig. 1B and Fig. S2) is robust between ensemble members. While various categorizations of “types” into functional groups might be considered, the classification here (Fig. 1B) reflects groupings of general interest and is tailored to reflect our particular interest in *Prochlorococcus*.

In general, the habitats of the emergent *Prochlorococcus*-analogues bear some qualitative resemblance to those observed but are much more sharply defined (Fig. 2, Fig. S4). Indeed, very low background abundances and sharply defined habitats of all the abundant, modeled phytoplankton types suggest that the model ecosystem is closer to complete competitive exclusion than is the real world (S23). This may reflect the relatively small number of

physiological specializations (niche dimensions) in the model, the comparatively smooth, coarse resolution, physical environment (S24) or the low diversity of predatorial strategies (S23).

Though each of the ten members of the ensemble of solutions are initialized with different randomization of the characteristics of the phytoplankton population, the emergent community structures and biogeography are relatively robust. For example, in each solution the four most abundant, emergent *Prochlorococcus*-analogs are relatively consistent (Fig. S3): the most abundant is typically of *m-e1* classification and the second most abundant typically *m-e2*, with *m-e3* type analogs at lower abundances. Although our model does not exhibit a significant deep (low light) biomass of *Prochlorococcus*-analogs (Fig. S4), there is a deep biomass maximum at the nutricline in the equatorial regions, comprised of “other small phytoplankton” types. Some of the phytoplankton types which make up this deep maximum might represent nitrate consuming *Prochlorococcus* strains which have been suggested from field observations (S25) but not yet cultured. Such organisms, though present in the model, are not classified as *Prochlorococcus* in our rather crude definition of functional groups.

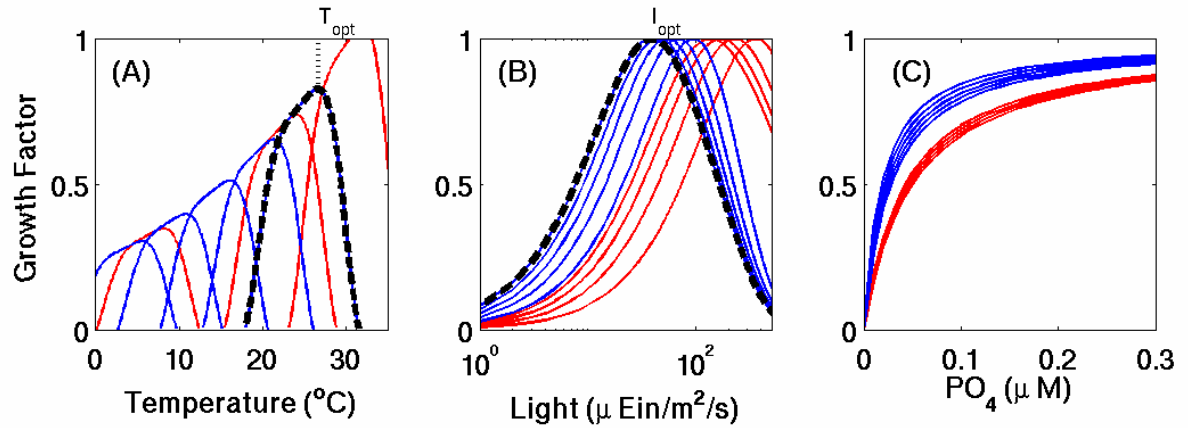


Fig. S1 Functional forms of the sensitivity of phytoplankton growth to (A) temperature, (B) flux of photosynthetically active radiation, and (C) ambient phosphate concentration expressed as normalized, non-dimensional growth factors, γ_j , which modulate the maximum intrinsic growth rate. The collection of curves in each panel is chosen to illustrate the ranges from initialized sensitivities are selected. Simple allometric trade-offs are indicated by the different ranges for the small phytoplankton class (blue curves) and large phytoplankton class (red curves). The highly idealized parameterization of light sensitivity captures variations in optimal light intensity but does not explicitly represent variability in the maximum light dependent growth factor. However, larger phytoplankton are given a higher intrinsic growth rate, μ_j . Optimal temperature and light intensity for growth, T_{opt} and I_{opt} , are illustrated for a single phytoplankton type (dashed black curves).

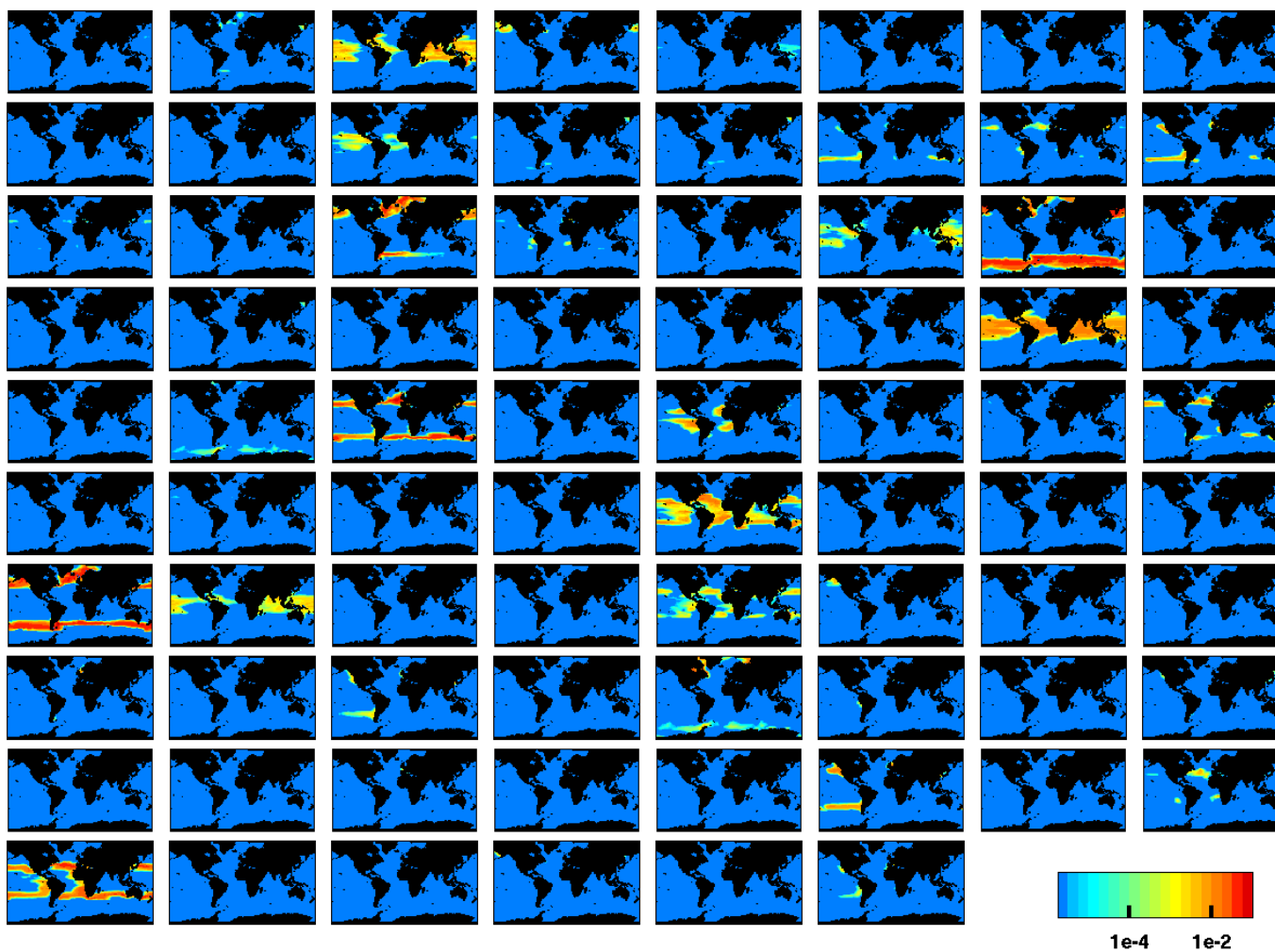


Fig. S2. Phytoplankton abundance ($\mu\text{M P}$; average 0-50m, logarithmic color-scale) for each of 78 initialized types in a single ensemble member. Annual mean of tenth year of integration.

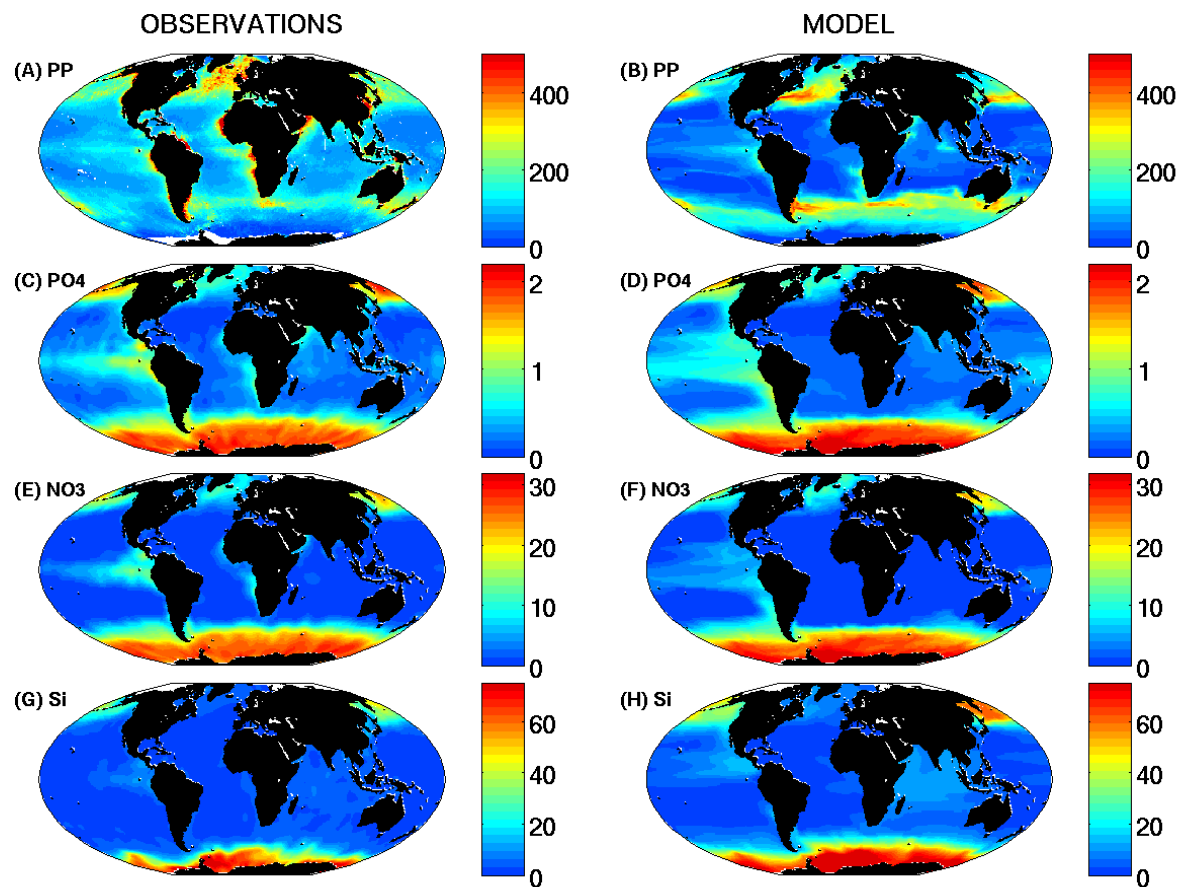


Fig S3: Comparison of one ensemble member annual (0-50m) fields (right column) to observations (left column). (A,B) Primary Production ($\text{gC}/\text{m}^2/\text{y}$); (C,D) Phosphate ($\mu\text{M P}$); (E,F) Nitrate ($\mu\text{M N}$); (G,H) Silicic Acid ($\mu\text{M Si}$). Observational euphotic layer primary production was calculated for 2005 using the Vertically Generalized Productivity Model (S26) and SeaWiFS-derived Chl. Data for this panel was downloaded from <http://science.oregonstate.edu/ocean.productivity>. Observational nutrients are from climatology of *in situ* data (S3) and are averaged over 0-50m.

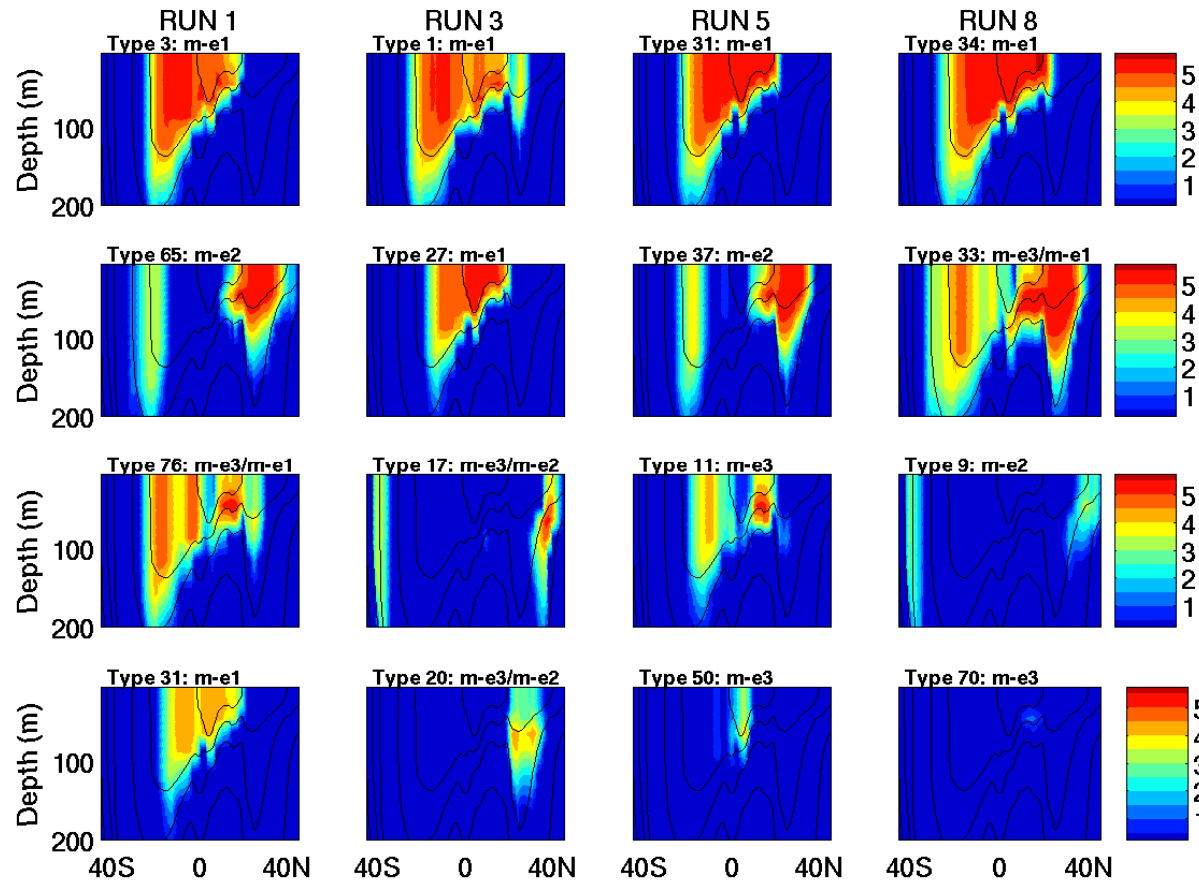


Fig. S4. The four most abundant *Prochlorococcus*-analogs ($\log(\text{cells } \text{m}^{-1})$) for the month of September along the AMT13 track from four of the ten member ensemble of integrations. “Type” number indicates the numerical designation of each of the 78 stochastically initialized phytoplankton types in each ensemble member. Analogs are classified into model-ecotypes as described in the main text. Model biomass is converted to cell density assuming a nominal phosphorus quota of 1 fg cell^{-1} for *Prochlorococcus* (13). Black contours are isotherms.

262 **Table S1: Parameters of the ecosystem model**

Parameter	Symbol	Fixed Value	Range	Units
Maximum phytoplankton growth rate	μ	Small: 1.4 Large: 2.2		d ⁻¹
Phytoplankton mortality rate	m^p	Small: 0.1 Large: 0.1		d ⁻¹
PAR saturation coefficient	k_{sat}		Small: mean 0.012, std 0.01 Large: mean 0.012, std 0.003	($\mu\text{Ein m}^{-1} \text{s}^{-1}$) ⁻¹
PAR inhibition coefficient	k_{inhib}		Small: mean $6*10^{-3}$, std $1*10^{-4}$ Large: mean $1*10^{-3}$, std $5*10^{-5}$	($\mu\text{Ein m}^{-1} \text{s}^{-1}$) ⁻¹
Temperature curve coefficient	A	1.04		
Temperature optimum coefficient	T_o		-2 to 30	°C
Temperature range coefficient	B	Small: $1*10^{-3}$ Large: $3*10^{-4}$		°C ⁻¹
Temperature decay coefficient	C	4		
Temperature normalization coefficients	τ_1, τ_2	0.33, 0.3		
Phosphate half saturation	K_{PO4}		Small: $1.35*10^{-2}$ to $3.5*10^{-2}$ Large: $3.5*10^{-2}$ to $5.5*10^{-2}$	$\mu\text{M P}$
Nitrate half saturation	K_{NO3}		Small: 0.24 to 0.56 Large: 0.56 to 0.88	$\mu\text{M N}$
Nitrite half saturation	K_{NO2}		Small: 0.16 to 0.42 Large: 0.42 to 0.66	$\mu\text{M N}$
Ammonium half saturation	K_{NH4}		Small: $4.3*10^{-2}$ to 0.112 Large: 0.112 to 0.132	$\mu\text{M N}$
Silicic acid half saturation	K_{si}		Non-diatom: 0 Diatom: 2	$\mu\text{M Si}$
Iron half saturation	K_{Fe}		Small: $1.7*10^{-5}$ to $4.4*10^{-5}$ Large: $4.4*10^{-5}$ to $6.9*10^{-5}$	$\mu\text{M Fe}$
Phytoplankton elemental ratios	$R_{Si:P}$ $R_{N:P}$ $R_{Fe:P}$	16 16 $1.25*10^{-3}$		
Ammonia/nitrite inhibition	ψ	4.6		($\mu\text{M N}$) ⁻¹
Nitrate consumption cost	v	0.1		
Phytoplankton sinking rate	w^p	Small: 0 Large: 0.5		m d ⁻¹
Phytoplankton partitioning DOM/POM	f_{DOM}	Small: 0.2 Large: 0.5		

Zooplankton fast grazing rate	g_{fast}	0.2		d ⁻¹
Zooplankton slow grazing rate	g_{slow}	0.033		d ⁻¹
Zooplankton mortality rate	m^z	0.033		d ⁻¹
Phytoplankton half saturation	K^p	0.1		μM P
DOM remineralization rate	r_{DOP} r_{DON} r_{DOFe}	$2.8*10^{-3}$ $2.8*10^{-3}$ $2.8*10^{-3}$		d ⁻¹
POM remineralization rate	r_{POP} r_{PON} r_{POFe} r_{POSi}	0.033 0.033 0.033 $3.3*10^{-3}$		d ⁻¹
POM sinking rate	w_{POM}	10		m d ⁻¹
NH ₄ to NO ₂ oxidation rate	ζ_{NO2}	0.1		d ⁻¹
NO ₂ to NO ₃ oxidation rate	ζ_{NO3}	0.033		d ⁻¹
Iron solubility constant	α_{Fe}	0.04		
Iron scavenging rate	c_{Fe}	$1.1*10^{-3}$		d ⁻¹
Ligand binding strength	β_{Fe}	$2*10^5$		(μM Fe) ⁻¹
PAR attenuation coefficient	k_o	0.04		m ⁻¹
PAR attenuation coefficient from phytoplankton	k_{phyto}	0.64		(μM P) ⁻¹ m ⁻¹

SUPPORTING REFERENCES:

- S1. C. Wunsch, P. Heimbach, *Physica D*, doi:10.1016/j.physd.2006.09.040 (2006).
- S2. J. Marshall *et al.*, *J. Geophys. Res.*, **102**, 5733 (1997).
- S3. M.E. Conkright *et al.*, *World Ocean Atlas 2001*: vol. 4, *Nutrients*, NOAA Atlas NESDIS 52, NOAA, Silver Springs, MD (2002).
- S4. S. Dutkiewicz, M.J. Follows, P. Parekh, *Global Biogeochem. Cycles*, **19**, GB1021, doi:10.1029/2004GB002342 (2005).
- S5. G. Riley, *J. Marine Res.*, **6**, 54 (1946).
- S6. M.J.R. Fasham, H.W. Ducklow, D.S. McKelvie, *J. Marine Res.*, **48**, 591 (1990).
- S7. W.W. Gregg, P. Ginoux, P.S. Schopf, N.W. Casey, *Deep-Sea Res. II*, **50**, 3143 (2003).
- S8. L.R. Moore, A.F. Post, G. Rocap, S.W. Chisholm, *Limnol. Oceanogr.*, **47** 989 (2002).
- S9. J. Wroblewski. *Mar. Res.*, **35**, 357 (1977).
- S10. P.A. Thompson, M.E. Levasseur, P.J. Harrison, *Limnol. Oceanogr.*, **34**, 1014 (1989).
- S11. R.W. Epply, *Fisheries Bull.*, **70**, 1063 (1972).
- S12. T. Platt, C.L. Gallegos, W.G. Harrison, *J. Mar. Res.*, **38**, 687 (1980).
- S13. S. Bertilsson, O. Berglund, D.M. Karl, S.W. Chisholm, *Limnol. Oceanogr.*, **48**, 1721- (2003).
- S14. M.R. Droop, *J. Mar. Bio., Ass. U.K.*, **54**, 825 (1974).
- S15. J. Caperon, *Ecology*, **49**, 866 (1968).
- S16. E.A. Laws, *Ecology*, **56**, 419 (1975).
- S17. J. Gavis, *J. Marine Res.*, **34**, 161 (1976).
- S18. J. Raven, P.G. Falkowski, *Aquatic Photosynthesis*, Blackwell (1997).
- S19. Z.V. Finkel, *Limnol. Oceanogr.*, **46**, 86 (2001).
- S20. P. Parekh, M.J. Follows, E.A. Boyle, *Global Biogeochem. Cycles*, **18**, GB1002, doi:10.1029/2003GB002061 (2004).
- S21. N. Mahowald, C. Lou, J. del Corral, C. Zender, *J. Geophys. Res.*, **108**, doi:10.1029/2002JD002821 (2003).
- S22. A.R. Longhurst, *Ecological Geography of the Sea*. Academic Press. 398pp (2001).
- S23. G.E. Hutchinson, *American Naturalist*, **95**, 137 (1961).
- S24. S. Tozzi, O. Schofield, P. Falkowski, *MEPS*, **274**, 123 (2004).
- S25. M.W. Lomas, F. Lipschultz, *Limnol. Oceanogr.*, **51**, 2453 (2006).
- S26. M.J. Behrenfeld, P.G. Falkowski, *Limnol. Oceanogr.*, **42**, 1479 (1997).

Supporting Online Material

www.sciencemag.org

Methods

Supporting Text

Figs. S1, S2, S3, S4

Table S1